Chemical Engineering Journal 480 (2024) 147962

Contents lists available at ScienceDirect

Chemical Engineering Journal

journal homepage: www.elsevier.com/locate/cej

# High-performance flexible organic gas sensor via alkyl side chain engineering of polyalkylthiophene

Ming Hong, So Young Park, Ji Eun Lee, Yeong Don Park *

*Department of Energy and Chemical Engineering, Incheon National University, Incheon 22012, Republic of Korea*

ARTICLE INFO

*Keywords:*
OFET
Gas sensor
Alkyl side chain
P3AT
$NO_2$

ABSTRACT

Poly(3-alkylthiophene) (P3AT) is a representative p-type organic semiconductor with a distinctive molecular structure that incorporates a π-electron system, promoting charge carrier mobility and providing exceptional electrical conductivity. The alkyl side chain linked to the π-electron backbone was found to have a significant effect on charge carrier transport and mechanical properties. This study presents a comprehensive comparison of the gas-sensing performances of various gases ($NO_2$, $SO_2$, and $CO_2$) and the mechanical properties of gas sensors fabricated from P3AT with alkyl chain lengths of 6, 8, 10, and 12 (P3HT, P3OT, P3DT, and P3DDT). Our investigations revealed that as the alkyl side chain length increased, the gas sensor performance significantly improved owing to the increase in free volume, concurrently promoting improved flexibility. The P3DDT sensor exhibited a sensitivity approximately twice that of the P3HT sensor, along with superior mechanical flexibility owing to its free volume.

## 1. Introduction

Air pollution is a critical environmental issue globally. The World Health Organization (WHO) estimates a staggering annual death toll of approximately 7 million people worldwide because of the deleterious effects of air pollution [1,2]. Consequently, the significance of gas-sensing technology has surged in various domains, including environmental detection [3–8], industrial safety [9–12], health diagnosis [13–17], and intelligent equipment [18–20]. The demand for portable gas-sensing technology with high sensitivity and selectivity has become particularly urgent.

Among the myriad gas-sensing technologies, organic transistor sensors have garnered substantial attention as a promising and emerging approach, owing to their inherent simplicity, cost-effectiveness, and remarkable lightness. Notably, poly-3-alkylthiophene (P3AT) materials have gained prominence in organic electronics owing to their excellent electrical properties and desirable characteristics [21–27]. These materials feature a thiophene ring structure that facilitates efficient packing in the crystalline lattice. This arrangement promotes the planarity of the thiophene rings along the main chain and allows for the effective overlap of their π orbitals. These attributes are critical factors facilitating efficient charge transport [28].

On the other hand, the presence of long alkyl side chains provides greater conformational freedom to P3AT materials, thereby heightening the entropy driving force for solubility and consequently increasing solubility. The alkyl side chain, a crucial structural component of the P3AT molecule, has a significant effect on various material properties, such as morphology, crystal structure, intermolecular interactions, carrier migration, and mechanical properties [29–31]. Long alkyl side chains with insulating properties have been observed to induce a downward highest occupied molecular orbital (HOMO) energy level shift, resulting in a higher hole injection barrier and thereby reducing hole mobility, which can have implications for the efficiency of charge transport within the material [32,33]. Despite the paramount importance of alkyl side chain length in P3AT materials, the comprehensive impact of alkyl side chain length on gas-sensing performance and mechanical properties remains insufficiently investigated. In organic field-effect transistors (OFETs), it is known that a short alkyl chain improves charge carrier transport [34–36]. Further research is needed to gain a more profound understanding of how the alkyl side chain length can be manipulated to optimize the performance of organic transistor gas sensors, taking into account both sensing capabilities and mechanical stability.

This study primarily aims to systematically investigate the sensing performance and mechanical properties of OFET-based gas sensors using different alkyl side chain lengths (6, 8, 10, and 12) represented by P3HT,

* Corresponding author.
*E-mail address:* ydpark@inu.ac.kr (Y.D. Park).

https://doi.org/10.1016/j.cej.2023.147962
Received 6 October 2023; Received in revised form 30 November 2023; Accepted 6 December 2023
Available online 10 December 2023

P3OT, P3DT, and P3DDT, respectively, and the chemical structure of P3AT is shown in Fig. 1a. Notably, the alkyl side chains caused significantly different morphologies and molecular orders in the films, resulting in different charge-carrier transport and mechanical properties. Through a thorough analysis, our study provides valuable insights for optimizing P3AT-based sensor designs.

## 2. Results and discussion

### 2.1. Morphology of P3AT film

The P3AT solution was spin-coated onto a silicon substrate, and the surface morphology of the P3AT film was investigated in relation to the length of the alkyl side chain. All the P3AT films exhibited uniform morphologies under an optical microscope (Fig. 1a). Atomic force microscopy (AFM) was used to further explore the surface profile and nanoscale morphology. Fig. 1b and 1c show the height and phase images of the films, respectively. The AFM analysis revealed that the P3HT film exhibited the highest surface roughness, with a measured surface roughness of 0.852 nm. In contrast, as the length of the alkyl side chain increased, the surface roughness of the films gradually decreased. Notably, the P3DDT film exhibits the smoothest surface characteristics, with a surface roughness of 0.503 nm. Brighter areas in the phase images indicate regions with higher rigidity, whereas darker areas correspond to regions with greater softness. This discernible trend indicates that longer alkyl side chains create a greater free volume between the molecular chains, resulting in increased film softness [37].

UV–Vis absorption spectroscopy was used to assess the impact of the alkyl side chain length on the molecular states and crystalline order of the P3AT films. In Fig. 2a, the absorption spectra of all P3AT films exhibited three main absorption bands: the intra-chain π-π* transition peak $A_{0-2}$ (λ ≈ 520 nm), the first transition peak $A_{0-1}$ (λ ≈ 558 nm), and the second transition peak $A_{0-0}$ (λ ≈ 605 nm), corresponding to the interchain π-π interaction. Fig. 2b illustrates a summary of the calculated crystallinities and film thicknesses. The determination of P3AT crystallinity was based on the peak intensity ratio of peaks $A_{0-0}$ and $A_{0-2}$, while the film thickness was evaluated using the Beer-Lambert law [38,39]. Notably, the thickness of all films was consistently found to be approximately 70 nm. Because the P3AT film was spin-coated using a chloroform with a low boiling point, the all P3AT film showed low crystallinity. However, the P3HT film exhibited the highest value of $A_{0-0}/A_{0-2}$, indicating that it had the highest degree of crystallinity. As the length of the alkyl side chains increased, the value of $A_{0-0}/A_{0-2}$ decreased, indicating a reduction in the film crystallinity. This observation aligns with the findings of the AFM analysis, in which the P3DDT film demonstrated the lowest crystallinity. Similarly, the observed correlation between decreased crystallinity and increased alkyl side chain length can be attributed to the augmented free volume provided by longer alkyl side chains. The long alkyl chains increase the distance between the polymer backbones, which increases the free volume and disorder within the film.

To investigate the variations in the molecular structure in the P3AT films, we carried out grazing incidence X-ray diffraction (GIXD) measurements. Fig. 2c,d shows the out-of-plane GIXD patterns of P3AT films. Both the out-of-plane 100 reflection due to the lamellar layer structure and the out-of-plane 010 reflection due to interchain stacking are very weak. As the alkyl side chains increase, the GIXD peak gradually decreases and is not observed in the P3DDT film. These GIXD results showed the same trend as UV–Vis absorption spectroscopy.

The backbone packing density within the P3AT films was determined through the analysis of X-ray photoelectron spectroscopy (XPS) data. Fig. 2e,f show the high-resolution detailed spectra of C 1s and S 2p, respectively. Intriguingly, as the length of the alkyl side chain increased from 6 to 12 carbons, a gradual decrease in the peak intensities of C 1s and S 2p peak was observed. This can be attributed to the fact that P3HT films with short alkyl side chains are well-crystallized owing to the short distances between the backbones, in which the chain packing density is high and the free volume is reduced. Therefore, the higher the packing density, the more pronounced the C 1s and S 2p peaks in the XPS spectra, indicating a greater degree of molecular ordering and structural

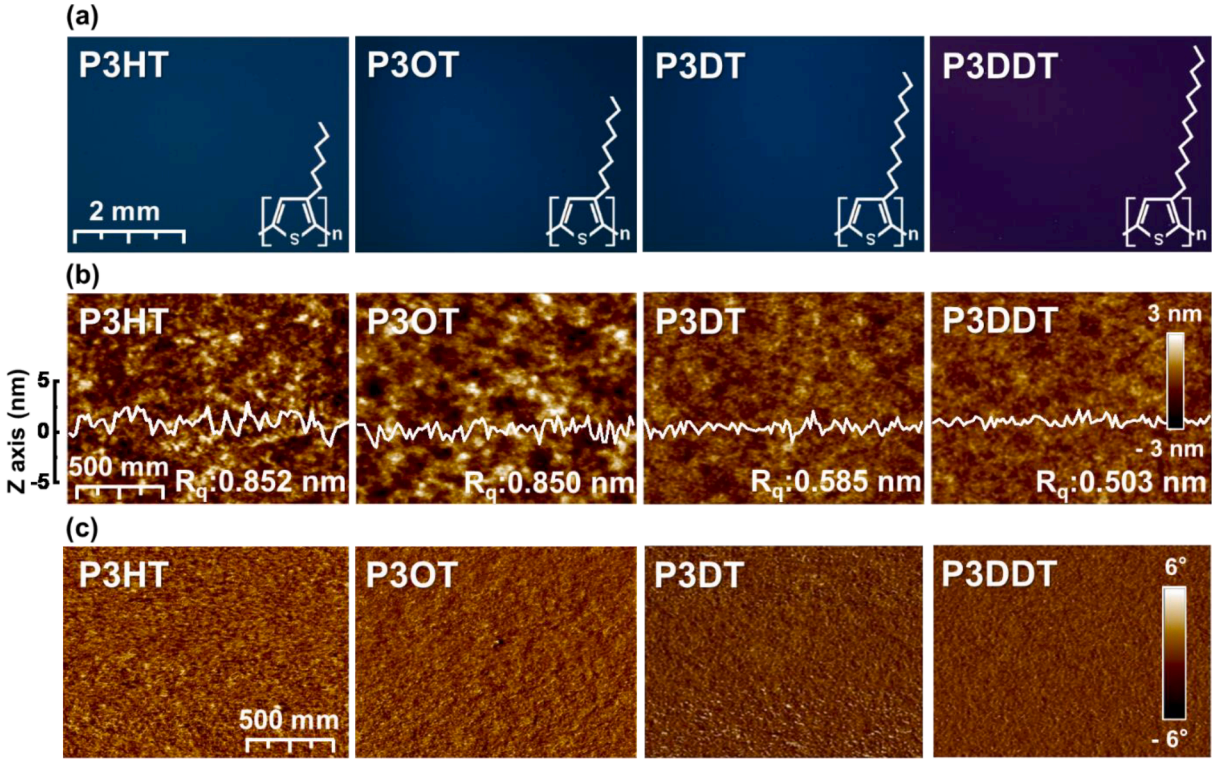


**Fig 1.** (a) OM images of the P3AT film with the chemical structure diagram. (b) Height and mean square roughness ($R_q$) of the P3AT films surface by AFM. (c) Phase images of the P3AT films surface by AFM.

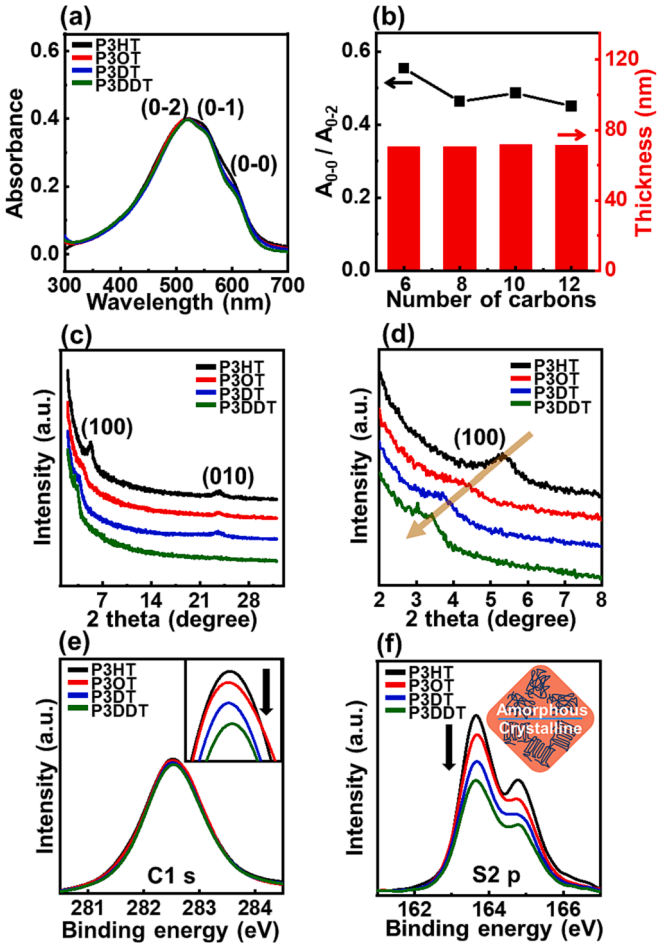


**Fig 2.** (a) UV–Vis absorption spectra of the P3AT films. (b) Crystallinity and thickness were calculated from the 0–2 peak of the P3AT films. (c) Out-of-plane GIXD patterns for P3AT films with alkyl chain length. (d) Magnified (1 0 0) peak of P3AT films with alkyl chain length. High-resolution XPS spectra of the P3AT film: (e) C 1s, (f) S 2p.

regularity. In contrast, the P3DDT molecules have a long distance between their backbones owing to their long alkyl side chains, resulting in more amorphous regions in the film, reduced packing density, and increased free volume. Consequently, the lower intensity of the C 1s and S 2p peaks in the XPS spectra indicates a lower level of molecular order with a high free volume. The observed packing density and free volume in the P3AT film are expected to have implications for charge carrier transport, gas permeation, and mechanical properties, which are discussed below.

### 2.2. OFET performance of the P3AT

To determine the charge transport characteristics of the OFETs with varying alkyl side chain lengths of P3AT, we fabricated bottom-gate and top-contact transistors on $SiO_2$/Si substrates, as depicted in Fig. 3a. The transfer curves reflecting the charge transport properties of the OFETs are shown in Fig. 3b. The field-effect mobility (μ) and turn-on–off current ratio were calculated from the saturation region shown in Fig. 3c. Remarkably, as the alkyl side chain length increased, the drain current level exhibited a gradual downward shift, accompanied by a significant decrease in both the field-effect mobility and the turn-on–off current ratio. Specifically, the field-effect mobility of the P3HT film was measured to be 0.002 $cm^2 V^{-1} s^{-1}$, whereas the P3DDT film exhibited a notably lower value at only 0.0001 $cm^2 V^{-1} s^{-1}$, which is 20 times lower. Simultaneously, the drain current level decreased from $10^{-7}$ to $10^{-8}$ A. This observed decrease in drain current is attributed to the extensive insulating region formed by the long alkyl side chains with insulating properties, leading to poor charge carrier transport. It is noteworthy that long alkyl side chains of the conjugated polymer can increase the internal resistance in the active layer, impeding charge carrier transport between polymer backbones [32]. And the substantial free volume due to the reduction in the crystallinity of the film also hinders carrier carrier transport, thereby contributing to diminished drain current. Consequently, the alkyl side chain of P3AT emerges as a critical determinant influencing overall electrical performance of the OFETs.

### 2.3. Gas sensing performances of P3AT film

The gas-sensing performance of the P3AT-based gas sensors in terms of alkyl side chain length was evaluated in a gas-filled chamber at room temperature. The fabricated gas sensor devices were exposed to repeated 20-s pulse injections of $NO_2$ gas at a reference concentration of 10 ppm, followed by an air purge recovery time of 200 s. Fig. 3d illustrates the curve of normalized source-drain current [$I_D(t)/I_D(0)$] change when both the drain voltage ($V_D$) and gate voltage ($V_G$) were set to −20 V. During exposure to the $NO_2$ gas environment, the drain currents of all sensor devices increased significantly, regardless of the length of the alkyl side chain. This observation can be attributed to the strong oxidizing nature of $NO_2$ gas, which acts as an electron-withdrawing agent, leading to an increase in the hole concentration within the P3AT active layer and, consequently, an increase in the drain current [43]. The responsivity, recovery rate, and response rate of the gas sensor devices were calculated from the first-exposure recovery cycle (Fig. 3e-f). The responsivity is defined as $R = \Delta I_D/I_{D0}$, and the response/recovery rates are defined as $\Delta R/\Delta t$. It is evident that as the alkyl side chain length increases, the sensing performance of the gas sensor devices gradually improves, with the P3DDT film exhibiting twice the sensitivity of the P3HT film. As shown in Fig. 3g, this enhancement can be attributed to the longer alkyl side chains, resulting in an amorphous state and large free volume within the active layer. The increased free volume facilitated the accessible penetration of gas molecules through the active layer, creating easier gas diffusion paths and providing more adsorption sites near the channel region. Consequently, the sensing capability of the gas sensor device based on P3DDT with long alkyl side chains was significantly enhanced.

Furthermore, Fig. 4a shows the dynamic response test results of the gas sensor devices as the $NO_2$ gas concentration varied from 10 to 50 ppm. As expected, the sensors with alkyl side chains exhibited varying degrees of enhancement in response to the $NO_2$ concentration, consistent with the findings from the previous pulse cycle test results. Among the fabricated gas sensor devices, the P3DDT sensor demonstrated the highest drain current modulation across the entire range of $NO_2$ concentration changes, indicating the best sensing performance. The sensitivity of the sensor was calculated from the responsivity slope as a function of $NO_2$ content, as shown in Fig. 3d and 3 g. With an increase in the gas concentration, the P3DDT sensor with the longest alkyl side chains exhibited greater response and sensitivity changes. The sensitivity of the P3DDT sensor to 50-ppm $NO_2$ gas was more than twice that of the P3HT sensor.

Selective detection is a crucial evaluation index for gas sensor devices. The dynamic response of the gas sensor was also tested in $SO_2$ and $CO_2$ gas environments, as shown in Fig. 4b, 4c, 4e, and 4f. Similar to the gas detection performance for $NO_2$, the P3DDT film with the longest alkyl chain had the highest sensitivity for $SO_2$ and $CO_2$. However, it is evident from the figures that while the fabricated gas sensor devices also responded to $SO_2$ or $CO_2$ gas, their responsivity and sensitivity were significantly lower than those to $NO_2$ gas, as depicted in Fig. 4g. This difference in the sensing performance can be attributed to the varying oxidation abilities of the gases, as shown in Fig. 4h. The strong oxidizing nature of $NO_2$ gas facilitates its electron-withdrawing ability, resulting in a more pronounced response in gas sensor devices. In contrast, the

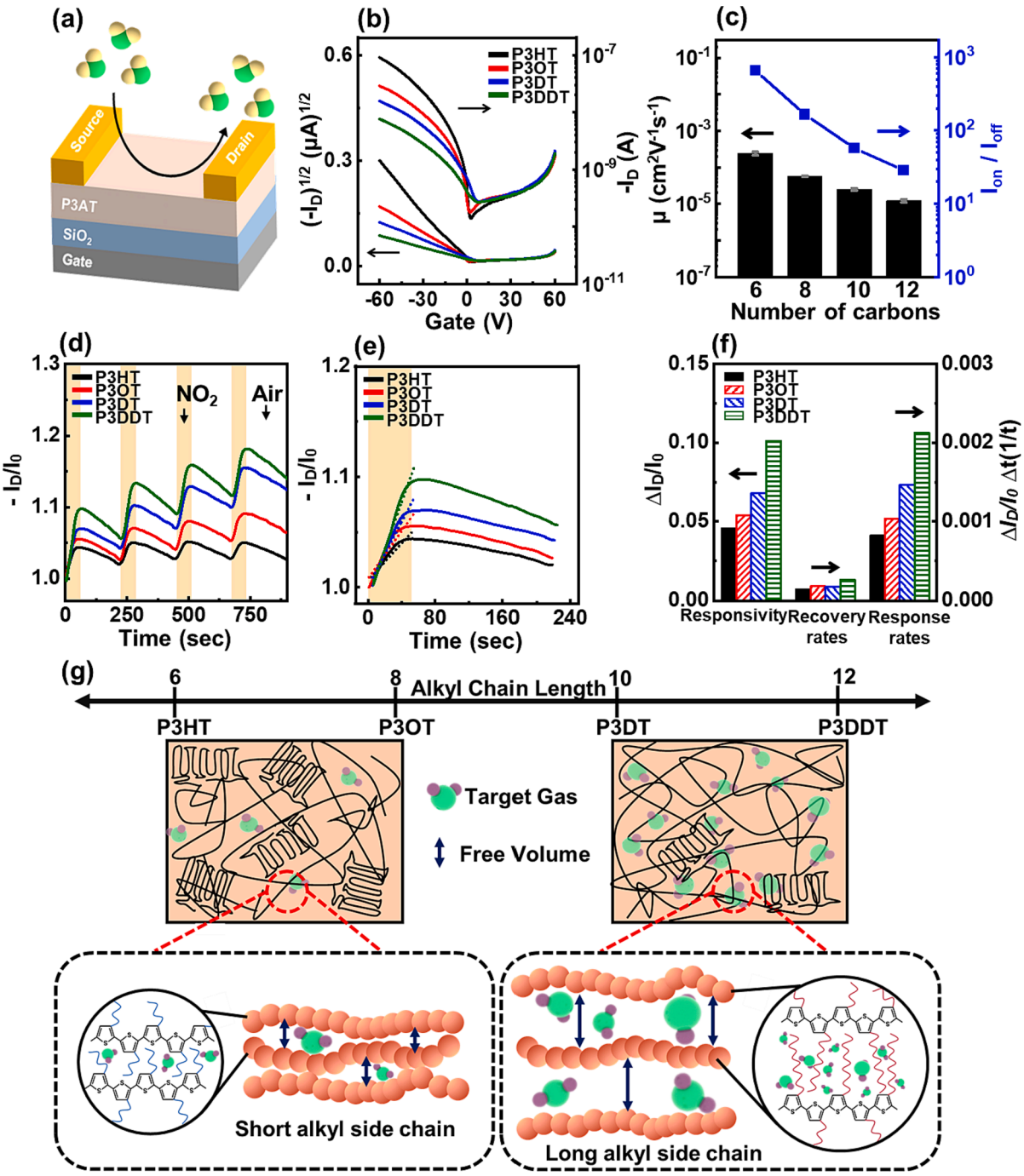


**Fig. 3.** (a) Schematic illustration of the OFETs-based gas sensors. (b) Plots of the $I_D$ as a function of $V_G$ at a fixed drain voltage ($V_D$ = − 60 V) for OFETs. (c) Field-effect mobility and the turn on–off current ratio for OFETs. (d) Repetitive gas sensing curves and (e) magnified first exposure-recovery cycle curves of gas sensor devices upon exposure to 10 ppm $NO_2$. (f) Calculated sensing parameters of gas sensor devices upon exposure to successive pulses of 10 ppm $NO_2$. (g) Schematic illustration delineating the distinct semicrystalline and amorphous regions within the film.

oxidation abilities of $SO_2$ and $CO_2$ gas are weaker than that of $NO_2$ gas, leading to diminished electron-withdrawing ability. Additionally, $CO_2$ molecules are nonpolar, resulting in fewer interactions, which significantly reduces their gas-sensing ability.

Consequently, compared to other gas sensor devices with shorter alkyl side chains, the P3DDT sensor showed a more sensitive and selective sensing ability for various harmful gases. We calculated a limit of detection (LOD) using methodologies detailed in previously published work, as outlined in the supplementary information. [44,45] The calculated limit of detection (LOD) results in Fig. 4i demonstrate that the P3DDT sensor has the highest sensitivity and lowest LOD for $NO_2$ gas, with values of 0.45 %/ppm and 0.26 ppt, respectively. This heightened sensitivity and selectivity implies that even under conditions involving multiple oxidizing mixed pollutant gases, an OFET-based gas sensor with a longer alkyl side chain can effectively detect sub-ppb concentrations of $NO_2$.

### 2.4. Mechanical property of P3AT film

To evaluate the mechanical properties of the P3AT films with varying alkyl side chain lengths, a stretching test was conducted on the P3AT films at tensile strains of 10 %, 30 %, 50 %, 70 %, and 100 %, along with

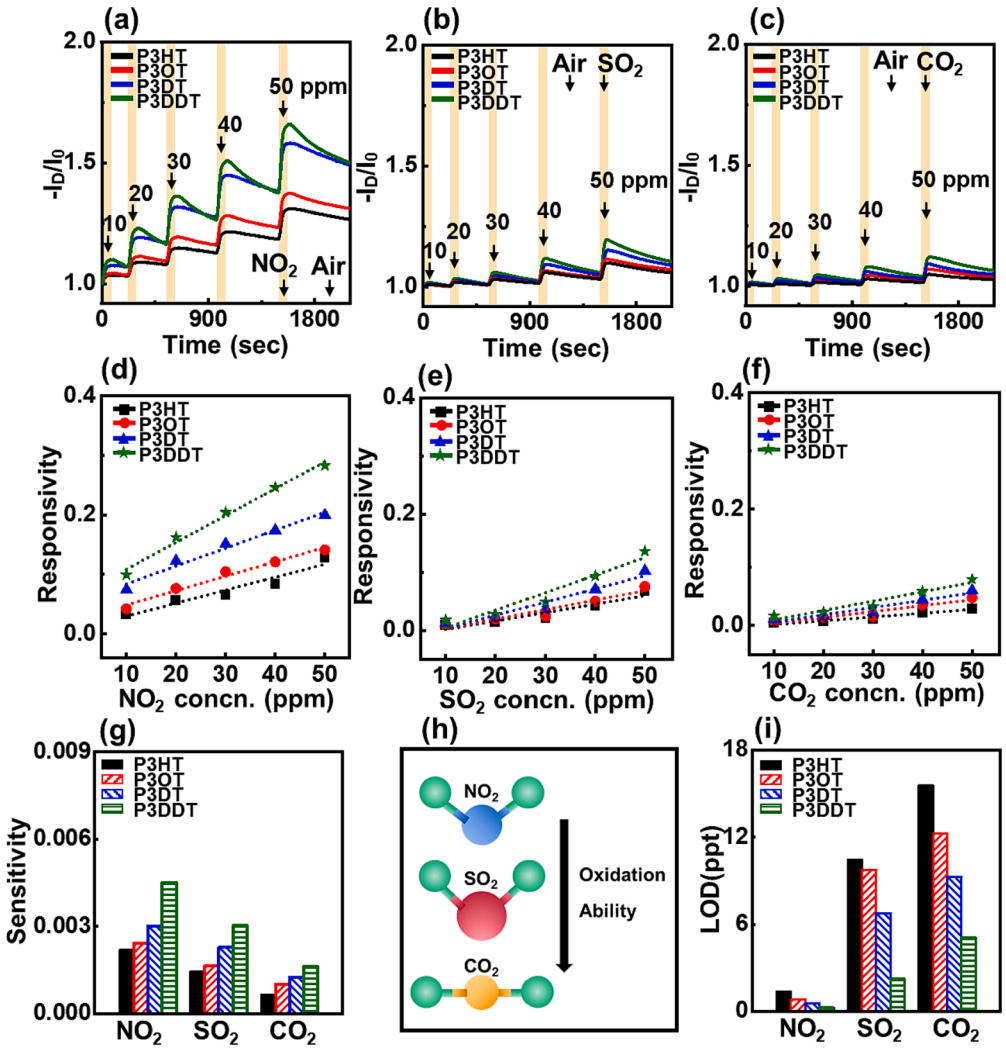


**Fig 4.** Repetitive gas sensing curves upon exposure to (a) $NO_2$ (b) $SO_2$ and (c) $CO_2$ at various concentrations from 10 to 50 ppm. (d-f) Linear fit showing the relative responsivity and the sensitivity is calculated from the slope of the linear fitted graphs. (g) Sensitivity of gas sensors calculated from the slope of the linear fitted graphs for various gases. (h) Schematic illustration depicting the various gases. (i) Limit of the detection value of gas sensors for various gases.

a bending test with a radius of 5 mm in both directions using mechanical equipment (Fig. 5a). The OM images after stretching presented in Fig. 5b are consistent with the AFM test results, showing that the P3DDT film with the longest alkyl side chains exhibited the highest flexibility. The P3HT film first cracked at 30 % tensile strain, followed by the P3OT film cracking at 50 % tensile strain. Both the P3DT and P3DDT films with longer alkyl side chains exhibited cracks after being stretched to 100 % tensile strain. As mentioned before, this can be attributed to the fact that the P3DDT film with long alkyl side chains possesses the largest free volume, which increases the softness of the film and enables it to withstand stronger tensile strains.

Fig. 5c,d, and S1a–d depict the variations in charge carrier mobility and transfer curves following repeated bending cycles. Prior to subjecting the films to bending, a significant disparity in charge carrier mobility was evident, with the shortest-side-chain P3HT thin-film transistor displaying a carrier mobility approximately ten times higher than that of the P3DDT thin film, characterized by the longest side chains. Remarkably, even after subjecting the films to as many as 1000 bending cycles, the charge-carrier mobility maintained its original value in all cases. However, after 1000 bending cycles, a pronounced reduction in charge carrier mobility was observed in the P3HT and P3OT films, which were characterized by shorter side chains. This decline persisted until the charge carrier mobility dropped below that of the P3DDT film after 4000 bending cycles. In contrast, the P3DDT films with the longest side chains consistently retained their charge carrier mobilities with minimal deviations, even after 4000 bending cycles. Furthermore, the gas sensing performance in the P3DDT film was found to decrease slightly after bending cycles, remaining almost at the initial value. As previously explained, this phenomenon can be attributed to the greater free volume within films featuring longer side chains, resulting in increased flexibility and mechanical properties and rendering them less vulnerable to the influence of external forces.

The glass transition temperature ($T_g$) and melting point ($T_m$) of P3AT, which are important factors that affect the mechanical properties of polymers, were analysed [46]. Fig. 5e illustrates the results of the differential scanning calorimetry (DSC) tests on P3AT. As the alkyl chain length increased, both the $T_g$ and $T_m$ of P3AT decreased (Fig. 5f and S1e–h). Specifically, $T_g$ decreased from −11 °C to −37 °C, and $T_m$ decreased from 219 °C to 149 °C. Polymers with a $T_g$ significantly lower than room temperature exhibits flexible mechanical characteristics. The presence of rigid π-conjugated backbones in P3AT restricts its conformational fluidity; however, the presence of alkyl chains caused a steric hindrance effect, increasing the free volume and configurational entropy between the π-conjugated main chains, reducing the van der Waals energy, and thereby lowering the activation energy required for chain-to-chain interaction [47]. P3AT films with a long alkyl side chain show

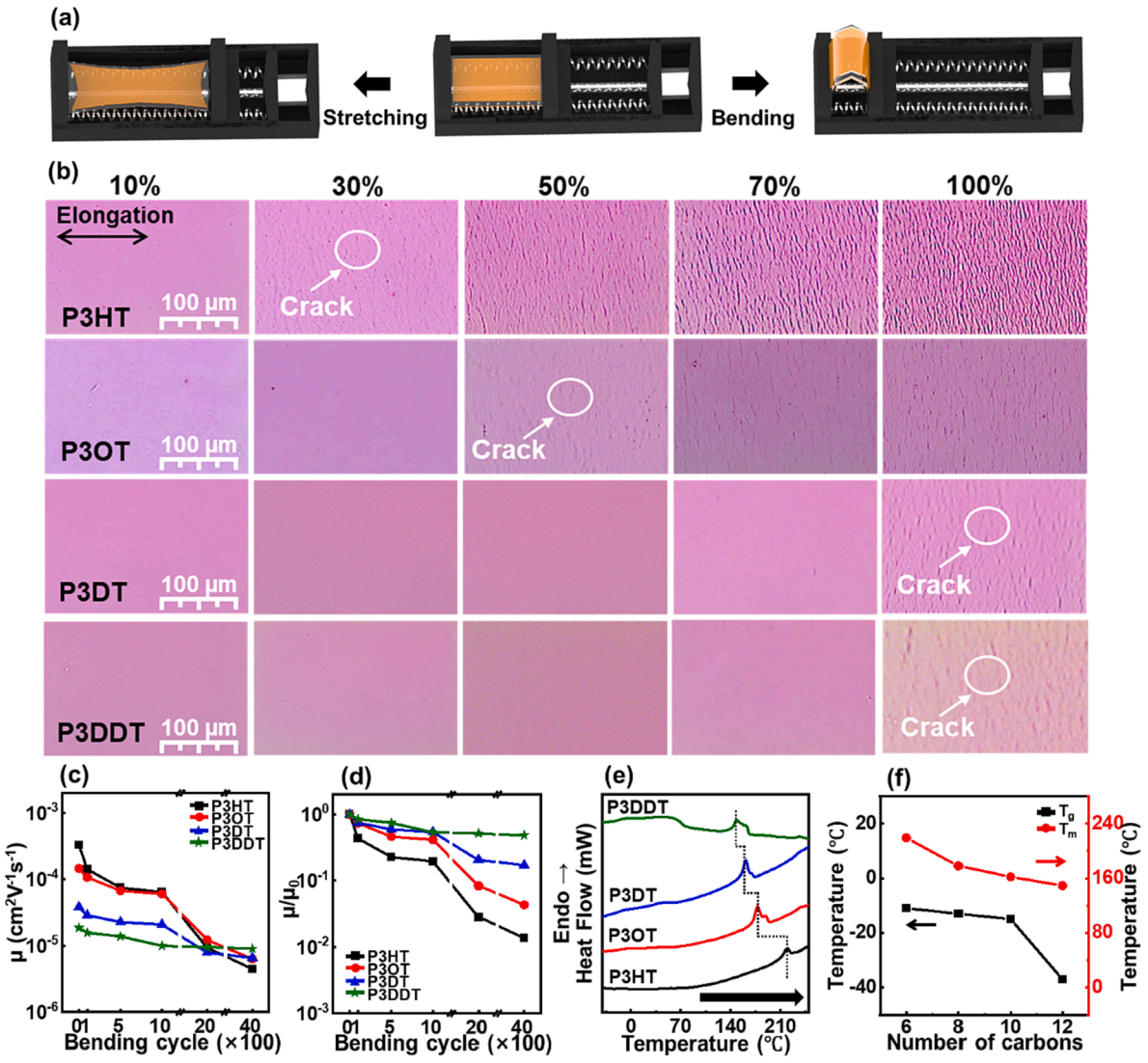


**Fig 5.** (a) Schematic representation of the tensile manipulator. (b) OM images of the stretched P3AT thin films. (c) Changes in the charge carrier mobility of the P3AT thin films as a function of the number of bending cycles. (d) Normalized charge carrier mobility. (e) DSC thermograms for P3AT. (f) $T_g$ and $T_m$ of P3AT as functions of side chain length.

excellent sensitivity and selectivity to oxidizing gases, as well as flexibility, which has potential for soft gas sensor applications.

## 3. Conclusion

In this study, the effects of alkyl side chains of varying lengths on the sensing performance and mechanical properties of P3AT (P3HT, P3OT, P3DT, and P3DDT) OFETs-based gas sensors were investigated. Our findings revealed that longer alkyl side chains decreased film crystallinity, reducing the charge mobility of OFETs. On the other hand, longer alkyl side chains also increase the amorphous region with a large free volume within the film, rendering it softer and more flexible. These characteristics allow for enhanced gas penetration and improved sensing capabilities of the gas sensor. Among the gas sensor devices, the P3DDT sensor containing the longest alkyl side chains exhibited remarkable sensing characteristics, with a sensitivity of 0.45 %/ppm and a LOD value of 0.26 ppt for $NO_2$ gas. This represents a two-fold enhancement in the sensing performance compared to that of the P3HT sensor, which contained the shortest alkyl side chains. In addition, the P3DDT sensor demonstrated superior selectivity toward $NO_2$ gas, underscoring its potential for specific gas detection applications. Overall, the findings of this study are expected to drive further advancements in organic transistor sensing technology, significantly contributing to the resolution of gas-monitoring challenges in environmental and health-related applications.

## 4. Experimental section

### 4.1. Preparation

In this study, regioregular polymers, specifically P3HT, P3OT, P3DT, and P3DDT, were purchased from Rieke Metals. These polymers showed regioregularity of 93 % for P3HT, 92 % for P3OT, and 91 % for both P3DT and P3DDT, respectively. The molecular weights ($M_W$) of these polymers varied, ranging from 45 kDa for P3HT and P3OT to 60 kDa for P3DT and P3DDT. To prepare the P3AT solutions, P3HT, P3OT, P3DT, and P3DDT powders were dissolved in chloroform. The concentrations of these solutions were meticulously adjusted to ensure uniform film thickness owing to their different solubilities. Through a series of methodical preliminary experiments, concentrations of 7 mg/ml, 8 mg/ml, 9.5 mg/ml, and 11.5 mg/ml were ascertained for P3HT, P3OT, P3DT, and P3DDT, respectively. The solution was then stirred at 550 rpm and 50 °C for 1 h to ensure complete dissolution, followed by an additional hour of stirring at room temperature for cooling and

stabilization.

The prepared P3AT solution was then spin-coated onto highly n-doped silicon wafers with a 300 nm-thick silicon dioxide layer. Prior to coating, the silicon wafers underwent continuous sonication cleaning in acetone and ethanol for 30 min each. Following the cleaning process, the cleaned wafers were exposed to UV ozone for 40 min before modification with hexamethylsilazane (HMDS). An HMDS organic interlayer was formed by spin-coating at 2500 rpm for 30 s and then baked at 130 °C for 1 h to ensure proper adhesion and uniformity. After cooling, the P3AT solution was spin-coated onto the HMDS-modified $SiO_2$/Si substrate at 2500 rpm for 60 s to form a uniform film. Additionally, for the UV–Vis measurements, the same process was replicated on a clean, transparent glass substrate to fabricate the P3AT film.

For the top-contact and bottom-gate OFETs, the source and drain electrodes were fabricated by vacuum-depositing 40 nm of Au under a shadow mask with a size of 2000 μm × 100 μm. To fabricate the gas sensor devices, silver paste and silver wire were used to wire the source and drain electrodes onto the sensor platform, establishing the necessary electrical connections and a conductive bridge between the active layer of the film and the external measurement circuitry.

For stretching testing, Ecoflex substrates were created by mixing Ecoflex prepolymers with their corresponding curing agents at weight ratios of 9:1 and 1:1. The P3AT-coated $SiO_2$ substrate was immersed in a hydrofluoric acid solution to remove the polymer film, which was then transferred to an Ecoflex substrate through a transfer process.

For the bending tests, a 70-nm thick Al electrode was deposited on the PET substrate as a gate via thermal evaporation. Subsequently, a 600 nm-thick parylene layer was deposited as the gate dielectric via chemical vapor deposition. The P3AT film was fabricated using an identical spin-coating procedure, and Au source and drain electrodes were subsequently deposited onto P3AT.

### 4.2. Characterization

The surface morphologies of the P3AT films were examined using optical microscopy (OM) and atomic force microscopy (AFM). The UV–Vis absorption spectra of the films were recorded using a Lambda 365 UV–Vis spectrophotometer (PerkinElmer) to analyze their molecular states and crystalline structures. The crystalline structure of the films was characterized by high-resolution X-ray diffraction (Smartlab, Rigaku). X-ray photoelectron spectroscopy (XPS, PHI 5000 Versa Probe II) was used to provide information on the surface elements of the films. The electrical properties of the OFETs were analyzed at room temperature in vacuum using a semiconductor analyzer (Keithley 4200-SCS) to measure the charge transport characteristics and field-effect mobility. Furthermore, the sensing performance of the gas sensor devices was evaluated at room temperature using a precision sensor system gas sensor (GASENTST) with both gate and drain voltages set to −20 V. In the pulse cycle sensing test, the gas concentration was maintained at 10 ppm, whereas in the dynamic cycle test, the gas concentration range varied from 10 to 50 ppm. Under all experimental conditions, gas was supplied from calibrated gas cylinders containing an air mixture. Finally, the mechanical properties of the P3AT films were assessed by stretching and bending tests using a reliable tensile manipulator (BM-100, ECOPIA). Tensile strains of 10 %, 30 %, 50 %, 70 %, and 100 % were applied to study the mechanical behavior of the films under different levels of stress. A series of continuous bending cycles comprising 100, 500, 1000, 2000, and 4000 repetitions was conducted, all of which were characterized by a consistent bending radius of 5 mm. These bending tests allowed the assessment of the impact of repeated bending on the electrical characteristics of the OFETs.

## CRediT authorship contribution statement

**Ming Hong:** Data curation, Formal analysis, Investigation, Writing – original draft, Writing – review & editing. **So Young Park:** Formal analysis, Investigation. **Ji Eun Lee:** Formal analysis, Investigation. **Yeong Don Park:** Conceptualization, Data curation, Funding acquisition, Project administration, Supervision, Writing – original draft, Writing – review & editing.

## Declaration of competing interest

The authors declare that they have no known competing financial interests or personal relationships that could have appeared to influence the work reported in this paper.

## Data availability

Data will be made available on request.

## Acknowledgements

This work was supported by the National Research Foundation of Korea (NRF) grant funded by the Korea government (MSIT) (No. NRF-2023R1A2C1005218).

## Appendix A. Supplementary data

Supplementary data to this article can be found online at https://doi.org/10.1016/j.cej.2023.147962.

## References

[1] S. Zikirillo, I. Ataboyev, Air pollution and control engineering and technology, Proc. Int. Conf. Modern Science Sci. Stud. (2023) 155–159.
[2] H. Xu, Y. Jia, Z. Sun, J. Su, Q.S. Liu, Q. Zhou, G. Jiang, Environmental pollution, a hidden culprit for health issues, Eco-Environ. Health 1 (1) (2022) 31–45.
[3] J. Lee, Y. Jung, S.-H. Sung, G. Lee, J. Kim, J. Seong, Y.-S. Shim, S.C. Jun, S. Jeon, High-performance gas sensor array for indoor air quality monitoring: the role of Au nanoparticles on WO 3, SnO 2, and NiO-based gas sensors, J. Mater. Chem. A 9 (2) (2021) 1159–1167.
[4] V. Kumar, D. Azhikodan, D.R. Roy, 2D Sb2C3 monolayer: a promising material for the recyclable gas sensor for environmentally toxic nitrogen-containing gases (NCGs), J. Hazard. Mater. 405 (2021), 124168.
[5] M. Mathew, C.S. Rout, Schottky diodes based on 2D materials for environmental gas monitoring: a review on emerging trends, recent developments and future perspectives, J. Mater. Chem. C 9 (2) (2021) 395–416.
[6] R.B. Onyancha, K.E. Ukhurebor, U.O. Aigbe, O.A. Osibote, H.S. Kusuma, H. Darmokoesoemo, V.A. Balogun, A systematic review on the detection and monitoring of toxic gases using carbon nanotube-based biosensors, Sens. Bio-Sens. Res. 34 (2021), 100463.
[7] J.B.L. Sanger, I. Sitanayah, A. Ahmad, Sensor-based Garbage Gas Detection System, in: IEEE, 2021, pp. 1347–1353.
[8] E. Traversa, M.L. Di Vona, S. Licoccia, M. Sacerdoti, M.C. Carotta, L. Crema, G. Martinelli, Sol-gel processed TiO2-based nano-sized powders for use in thick-film gas sensors for atmospheric pollutant monitoring, J. Sol-Gel Sci. Technol. 22 (2001) 167–179.
[9] Q. Li, W. Zeng, Y. Li, Metal oxide gas sensors for detecting NO2 in industrial exhaust gas: recent developments, Sens. Actuators B 359 (2022), 131579.
[10] F. Aliyu, T. Sheltami, Development of an energy-harvesting toxic and combustible gas sensor for oil and gas industries, Sens. Actuators B 231 (2016) 265–275.
[11] M.T. Carter, J.R. Stetter, M.W. Findlay, B.J. Meulendyk, V. Patel, D. Peaslee, Amperometric gas sensors: from classical industrial health and safety to environmental awareness and public health, ECS Trans. 75 (16) (2016) 91.
[12] A. Norman, F. Stam, A. Morrissey, M. Hirschfelder, D. Enderlein, Packaging effects of a novel explosion-proof gas sensor, Sens. Actuators B 95 (1–3) (2003) 287–290.
[13] X. He, H. Chai, Y. Luo, L. Min, M. Debliquy, C. Zhang, Metal oxide semiconductor gas sensing materials for early lung cancer diagnosis, J. Adv. Ceram. 12 (2) (2023) 207–227.
[14] L. Cai, X. Dong, G. Wu, J. Sun, N. Chen, H. Wei, S. Zhu, Q. Tian, X. Wang, Q. Jing, Ultrasensitive acetone gas sensor can distinguish the diabetic state of people and its high performance analysis by first-principles calculation, Sens. Actuators B 351 (2022), 130863.
[15] N.H. Hanh, L. Van Duy, C.M. Hung, C.T. Xuan, N. Van Duy, N.D. Hoa, High-performance acetone gas sensor based on Pt–Zn2SnO4 hollow octahedra for diabetic diagnosis, J. Alloy. Compd. 886 (2021), 161284.
[16] Q.A. Drmosh, I. Olanrewaju Alade, M. Qamar, S. Akbar, Zinc oxide-based acetone gas sensors for breath analysis: a review, Chemistry–an Asian Journal 16 (12) (2021) 1519–1538.
[17] V. Galstyan, Porous TiO2-based gas sensors for cyber chemical systems to provide security and medical diagnosis, Sensors 17 (12) (2017) 2947.

[18] Z. Song, W. Ye, Z. Chen, Z. Chen, M. Li, W. Tang, C. Wang, Z.a. Wan, S. Poddar, X. Wen, Wireless self-powered high-performance integrated nanostructured-gas-sensor network for future smart homes, ACS Nano 15 (4) (2021) 7659–7667.
[19] Z. Chen, Z. Chen, Z. Song, W. Ye, Z. Fan, Smart gas sensor arrays powered by artificial intelligence, J. Semicond. 40 (11) (2019), 111601.
[20] Y. Chen, D. Chen, T. Song, K. Song, An intelligent and portable air pollution monitoring system based on chemical sensor array, in: 2020 IEEE 4th International Conference on Frontiers of Sensors Technologies (ICFST), IEEE, 2020, pp. 21–25.
[21] S. Tiwari, S. Tiwari, R. Prakash, S. Balasubramanian, Study of electrical properties of poly-3-alkylthiophen (P3AT) derivatives P3HT, P3BT and P3DDT based field effect transistors annual, in: IEEE, 2013, pp. 1–4.
[22] J. Ficker, A. Ullmann, W. Fix, H. Rost, W. Clemens, Dynamic and lifetime measurements of polymer OFETs and integrated plastic circuits, Organic Field Effect Transistors, SPIE, 2001, pp. 95-102.
[23] J. Ficker, A. Ullmann, W. Fix, H. Rost, W. Clemens, Stability of polythiophene-based transistors and circuits, J. Appl. Phys. 94 (4) (2003) 2638–2641.
[24] E. Itoh, I. Torres, D. Taylor, The influence of interfacial charge exchange phenomena at the insulator-semiconductor interface on the electrical properties of poly (3-hexylthiophene) based field effect transistors, Jpn. J. Appl. Phys. 44 (1S) (2005) 641.
[25] M. Brinkmann, Structure and morphology control in thin films of regioregular poly (3-hexylthiophene), J Polym Sci B 49 (17) (2011) 1218–1233.
[26] H. Dong, C. Wang, W. Hu, High performance organic semiconductors for field-effect transistors, Chem. Commun. 46 (29) (2010) 5211–5222.
[27] T. Salammal Shabi, S. Grigorian, M. Brinkmann, U. Pietsch, N. Koenen, N. Kayunkid, U. Scherf, Enhancement in crystallinity of poly (3-hexylthiophene) thin films prepared by low-temperature drop casting, J. Appl. Polym. Sci. 125 (3) (2012) 2335–2341.
[28] S. Pankaj, M. Beiner, Long-term behavior and side chain crystallization of poly (3-alkyl thiophenes), Soft Matter 6 (15) (2010) 3506–3516.
[29] Z. Cao, L. Galuska, Z. Qian, S. Zhang, L. Huang, N. Prine, T. Li, Y. He, K. Hong, X. Gu, The effect of side-chain branch position on the thermal properties of poly (3-alkylthiophenes), Polym. Chem. 11 (2020) 517–526.
[30] K. Jiang, L. Wang, X. Zhang, Z. Ma, Y. Song, W. Zhang, Side-chain length dependence of young's modulus and strength in crystalline poly (3-alkylthiophene) nanofibers, Macromolecules 53 (22) (2020) 10061–10068.
[31] S. Pankaj, E. Hempel, M. Beiner, Side-chain dynamics and crystallization in a series of regiorandom poly (3-alkylthiophenes), Macromolecules 42 (3) (2009) 716–724.
[32] H.S. Lee, J.H. Cho, K. Cho, Y.D. Park, Alkyl side chain length modulates the electronic structure and electrical characteristics of poly (3-alkylthiophene) thin films, J. Phys. Chem. C 117 (22) (2013) 11764–11769.
[33] K. Takagi, T. Nagase, T. Kobayashi, H. Naito, High performance top-gate field-effect transistors based on poly (3-alkylthiophenes) with different alkyl chain lengths, Org. Electron. 15 (2) (2014) 372–377.
[34] T. Lei, J.-Y. Wang, J. Pei, Roles of flexible chains in organic semiconducting materials, Chem. Mater. 26 (1) (2014) 594–603.
[35] Y.D. Park, D.H. Kim, Y. Jang, J.H. Cho, M. Hwang, H.S. Lee, J.A. Lim, K. Cho, Effect of side chain length on molecular ordering and field-effect mobility in poly (3-alkylthiophene) transistors, Org. Electron. 7 (6) (2006) 514–520.
[36] B.C. Schroeder, T. Kurosawa, T. Fu, Y.C. Chiu, J. Mun, G.J.N. Wang, X. Gu, L. Shaw, J.W. Kneller, T. Kreouzis, Taming charge transport in semiconducting polymers with branched alkyl side chains, Adv. Funct. Mater. 27 (34) (2017) 1701973.
[37] A. Tamanai, S. Beck, A. Pucci, Mid-infrared characterization of thiophene-based thin polymer films, Displays 34 (5) (2013) 399–405.
[38] D.F. Swinehart, The beer-lambert law, J. Chem. Educ. 39 (7) (1962) 333.
[39] D. Calloway, Beer-lambert law, J. Chem. Educ. 74 (7) (1997) 744.
[43] Y.E. Hahm, S. Kweon, M.B. Park, Y.D. Park, Highly sensitive and selective organic gas sensors based on nitrided zsm-5 zeolite, ACS Appl. Mater. Interfaces 15 (5) (2023) 7196–7203.
[44] D. Jang, H. Jin, M. Kim, Y.D. Park, Polymeric interfacial engineering approach to perovskite-functionalized organic transistor-type gas sensors, Chem. Eng. J. 473 (2023), 145482.
[45] Y. Qin, X. Wang, J. Zang, Ultrasensitive ethanol sensor based on nano-Ag&ZIF-8 co-modified SiNWs with enhanced moisture resistance, Sens. Actuators B 340 (2021), 129959.
[46] A.J. Crosby, J.Y. Lee, Polymer nanocomposites: the "nano" effect on mechanical properties, Polym. Rev. 47 (2) (2007) 217–229.
[47] A.X. Chen, S.S. Pazhankave, J.A. Bunch, A. Lim, K. Choudhary, G.L. Esparza, R. Runser, C.G. Hoover, D.J. Lipomi, Adhesive properties of semiconducting polymers: poly (3-alkylthiophene) as an ersatz glue, Chem. Mater. 35 (8) (2023) 3329–3342.